NIKA2 observations of starless cores in Taurus and Perseus

C. Kramer[1,*], R. Adam[2], P. Ade[3], H. Ajeddig[4], P. André[4], E. Artis[5,6], H. Aussel[4], A. Beelen[7], A. Benoît[8], S. Berta[1], L. Bing[7], O. Bourrion[5], M. Calvo[8], P. Caselli[6], A. Catalano[5], M. De Petris[9], F.-X. Désert[10], S. Doyle[3], E. F. C. Driessen[1], G. Ejlali[11], A. Fuente[12], A. Gomez[12], J. Goupy[8], C. Hanser[5], S. Katsioli[13,14], F. Kéruzoré[15], B. Ladjelate[16], G. Lagache[7], S. Leclercq[1], J.-F. Lestrade[17], J. F. Macías-Pérez[5], S. C. Madden[4], A. Maury[4], P. Mauskopf[3,18], F. Mayet[5], A. Monfardini[8], A. Moyer-Anin[5], M. Muñoz-Echeverría[5], D. Navarro-Almaida[4], L. Perotto[5], G. Pisano[9], N. Ponthieu[10], V. Revéret[4], A. J. Rigby[19], A. Ritacco[20,21], C. Romero[22], H. Roussel[23], F. Ruppin[24], K. Schuster[1], A. Sievers[16], C. Tucker[3], and R. Zylka[1]

[1]Institut de RadioAstronomie Millimétrique (IRAM), 38406 Saint Martin d'Hères, France
[2]Université Côte d'Azur, Observatoire de la Côte d'Azur, CNRS, Laboratoire Lagrange, France
[3]School of Physics and Astronomy, Cardiff University, CF24 3AA, UK
[4]Université Paris-Saclay, Université Paris Cité, CEA, CNRS, AIM, 91191 Gif-sur-Yvette, France
[5]Université Grenoble Alpes, CNRS, Grenoble INP, LPSC-IN2P3, 38000 Grenoble, France
[6]Max Planck Institute for Extraterrestrial Physics, 85748 Garching, Germany
[7]Aix Marseille Univ, CNRS, CNES, LAM, Marseille, France
[8]Université Grenoble Alpes, CNRS, Institut Néel, France
[9]Dipartimento di Fisica, Sapienza Università di Roma, I-00185 Roma, Italy
[10]Univ. Grenoble Alpes, CNRS, IPAG, 38000 Grenoble, France
[11]Institute for Research in Fundamental Sciences (IPM), Larak Garden, 19395-5531 Tehran, Iran
[12]Centro de Astrobiología (CSIC-INTA), Torrejón de Ardoz, 28850 Madrid, Spain
[13]National Observatory of Athens, IAASARS, GR-15236, Athens, Greece
[14]Faculty of Physics, University of Athens, GR-15784 Zografos, Athens, Greece
[15]High Energy Physics Division, Argonne National Laboratory, Lemont, IL 60439, USA
[16]Instituto de Radioastronomía Milimétrica (IRAM), Granada, Spain
[17]LERMA, Observatoire de Paris, PSL Research Univ., CNRS, Sorbonne Univ., UPMC, 75014 Paris, France
[18]School of Earth & Space and Department of Physics, Arizona State University, AZ 85287, USA
[19]School of Physics and Astronomy, University of Leeds, Leeds LS2 9JT, UK
[20]INAF-Osservatorio Astronomico di Cagliari, 09047 Selargius, Italy
[21]LPENS, ENS, PSL Research Univ., CNRS, Sorbonne Univ., Université de Paris, 75005 Paris, France
[22]Department of Physics and Astronomy, University of Pennsylvania, PA 19104, USA
[23]Institut d'Astrophysique de Paris, CNRS (UMR7095), 75014 Paris, France
[24]University of Lyon, UCB Lyon 1, CNRS/IN2P3, IP2I, 69622 Villeurbanne, France

Abstract. Dusty starless cores play an important role in regulating the initial phases of the formation of stars and planets. In their interiors, dust grains coagulate and ice mantles form, thereby changing the millimeter emissivities and hence the ability to cool. We mapped four regions with more than a dozen cores in the nearby Galactic filaments of Taurus and Perseus using the NIKA2 camera at the IRAM 30-meter telescope. Combining the 1 mm to 2 mm flux ratio

*e-mail: kramer@iram.fr

maps with dust temperature maps from Herschel allowed to create maps of the dust emissivity index $\beta_{1,2}$ at resolutions of 2430 and 5600 a.u. in Taurus and Perseus, respectively. Here, we study the variation with total column densities and environment. $\beta_{1,2}$ values at the core centers ($A_V = 12 - 19$ mag) vary significantly between ~ 1.1 and 2.3. Several cores show a strong rise of $\beta_{1,2}$ from the outskirts at ~ 4 mag to the peaks of optical extinctions, consistent with the predictions of grain models and the gradual build-up of ice mantles on coagulated grains in the dense interiors of starless cores.

1 Cores in Taurus and Perseus

Herschel images of giant molecular clouds and dark cloud complexes have revealed large networks of filamentary structures where stars are born [1]. Filaments precede the onset of most star formation, funneling interstellar gas and dust into increasingly denser concentrations that will contract and fragment leading to gravitationally bound starless cores that will eventually form stars. In the cold dense interiors most molecules freeze-out [4, 8], covering the grains with icy mantles, which make them sticky, favoring grain coagulation, altering the grain size distribution, and their emissivity [14].

The dual-band camera NIKA2 [16] at the IRAM 30-meter telescope was used to map four regions in the nearby molecular filaments of Taurus and Perseus simultaneously at 1 and 2 mm wavelengths. The regions were selected from a survey of gas phase abundances in 29 starless cores covering different star formation activity, GEMS[1], a large program using the EMIR eight-band heterodyne receiver at the 30-meter telescope [6, 12]. The gas phase abundances of Carbon, Oxygen, Nitrogen, and Sulphur were measured together with the ionization fraction $X(e^-)$ by spatially resolved cuts of molecular key tracers through the cores.

The NIKA2 cores lie in Taurus and Perseus, two nearby filamentary molecular cloud complexes. The Taurus clouds show isolated low-mass star formation and lie at a solar distance of only 135 pc allowing us to reach resolutions of 2430 a.u. ($18''$) with NIKA2. The Perseus region exhibits the formation of stellar clusters and lies at a distance of 310 pc. Their cores sample a range of peak column densities parametrized by optical extinctions (12 to 19 mag), dust temperatures averaged along the lines of sight of 11 to 19 K, volume densities of $\sim 10^4$ to 10^5 cm^{-3} (Table 1), and gas phase fractional abundances. The cores are at different evolutionary stages and are located in different environments, from low-mass to massive star-forming regions. Different star formation activities translate into different UV fluxes and dust temperatures. Higher dust temperatures ($\sim$20 - 30 K) hinder the freeze-out of volatile molecules.

2 NIKA2 observations

The NIKA2 observations comprise 67.3 hours of telescope time. They were conducted in the years 2019 to 2022 in the framework of a series of open time proposals (027-19, 128-19, 006-20, 096-20, 010-21, 110-21, 008-22 (PI C. Kramer)). The total observed area covers more than 1000 arcmin^2 (Fig. 1). The average 1σ rms noise values are 0.3 mJy/beam at 2 mm and 0.9 mJy/beam at 1 mm. The NIKA2 observations were reduced adapting the `piic/gildas` pipeline provided by IRAM [2]. The average point source flux uncertainties during all runs are 6% at 2 mm and 8% at 1 mm, resulting in uncertainties of the ratios better than 10%. The relative calibration benefits from simultaneously observing under the same conditions and in particular through the same atmosphere.

---

[1]Gas phase Elemental abundances in Molecular clouds, https://www.oan.es/gems/doku.php, PI: A. Fuente.

Table 1. Properties of the cores observed with NIKA2: region, number of selected cores, range of peak optical extinctions, dust temperatures [21], volume densities [6, 11, 18], dust emissivities $\beta_{1,2}$ (this study, Figs. 1, 2). The last column lists the star formation activity of the region.

Region	#	A_V (mag)	T_d (K)	$n(H_2)$ $(10^4\,cm^{-3})$	$\beta_{1,2}$	SF activity
TMC1/Taurus	2	17-18	12-13	2-5	1.8-1.9	Low
B213/Taurus	2	15-17	11-12	5-6	1.8-2.3	Low
NGC1333/Perseus	6	12-17	12-19	5-11	1.1-1.9	Intermediate
IC348/Perseus	2	17-19	16-17	5-9	1.7-1.8	High
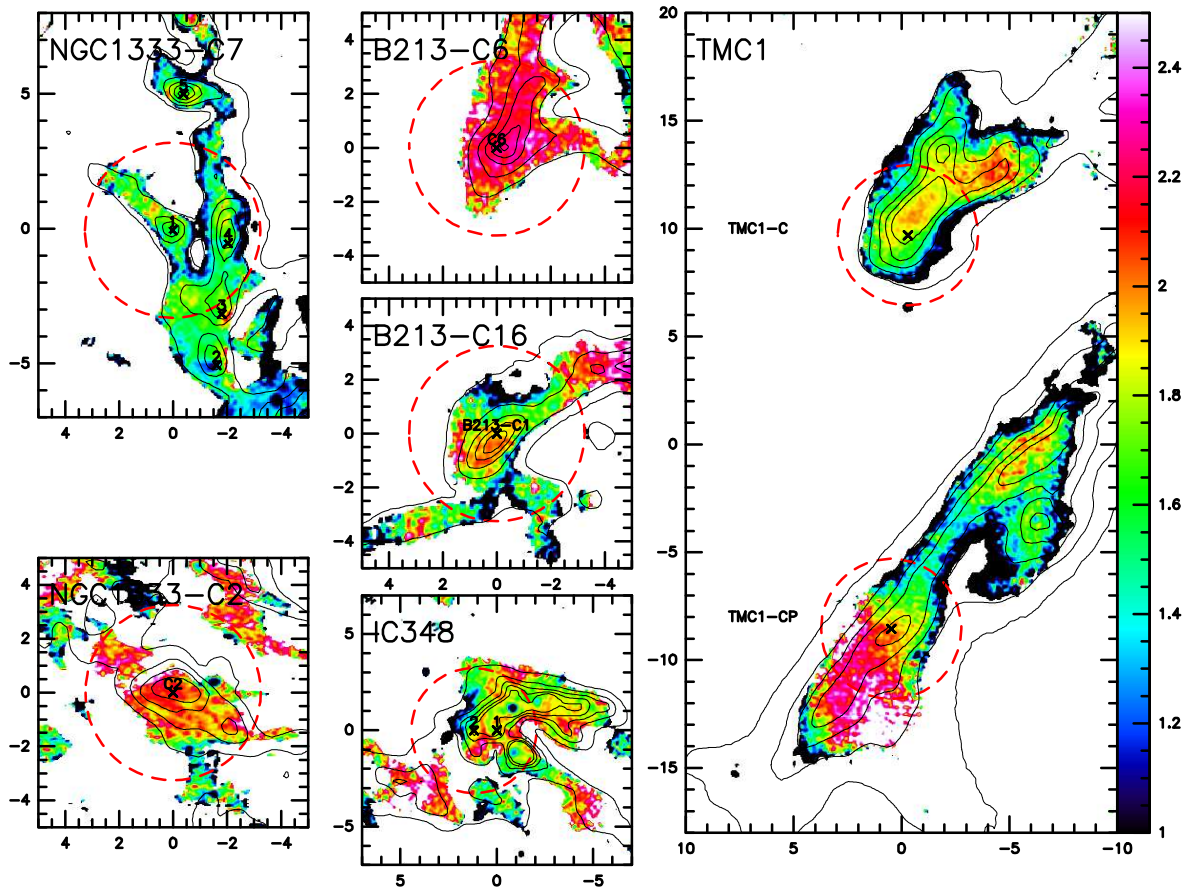
Figure 1. Maps of the dust emissivity index $\beta_{1,2}$ at a resolution of $18''$ for the regions mapped with NIKA2. Positions with fluxes below 6σ were masked. The range in $\beta_{1,2}$ is provided in the colour bar. Contours of optical extinctions are repeated at levels of 4, 7, 10, 13, 16 mag. Coordinates are ΔR.A. and ΔDec. offsets in arcminutes. The NIKA2 field-of-view of $6.5'$ is marked by red dashed circles. Black crosses mark the positions of selected cores (cf. Fig. 2).

3 The dust emissivity index

The observed intensities at a given frequency ν are given by $I_\nu = \tau_\nu B_\nu(T_d) = \kappa_\nu \Sigma B_\nu(T_d)$ with the opacity τ_ν, the Planck function B_ν, the dust temperature T_d, the emissivity cross section per gram of dust and gas κ_ν, and the gas surface density Σ. At the NIKA2 wavelengths, the assumption of optically thin emission is well justified. The emissivity cross section is often parametrized by $\kappa_\nu = \kappa_0 (\nu/\nu_0)^\beta$ introducing the long wavelength dust emissivity slope β. As
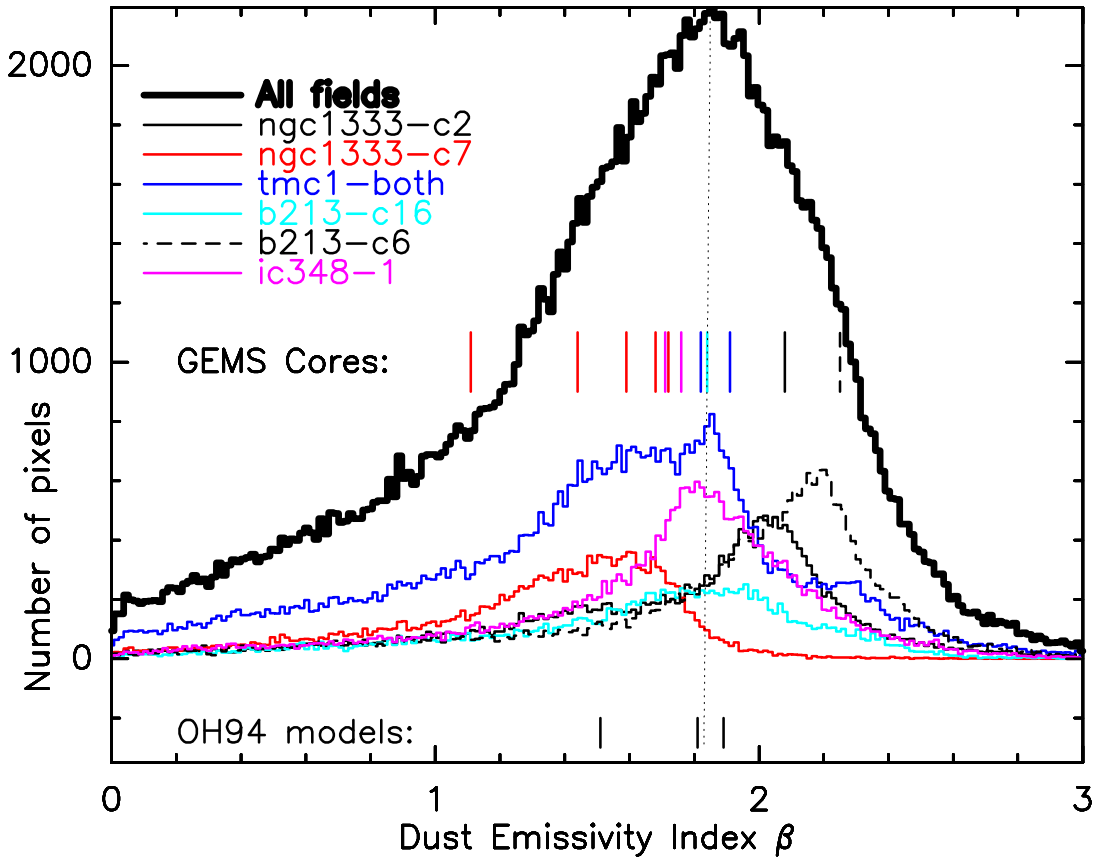
3

Figure 2. Number of map pixels per interval of the dust emissivity index $\beta_{1,2}$. The black histogram with thick lines shows the distribution for all regions with NIKA2 shown in Fig. 1, while the colored histograms show the distributions for each of the observed regions. Short, colored, vertical lines mark the beta values at the core centers. At the bottom, black vertical lines show that indices of OH94 grain models [15] for coagulated grains at $n_H = 10^5 \, \text{cm}^{-3}$ and varying the thickness of ice mantles (cf. Fig. 3, Right).

the Rayleigh-Jeans approximation is no longer valid at the low temperatures encountered in prestellar cores, the 1 mm/2 mm flux ratio $R_{1,2}$ is weakly dependent on the dust temperature: $R_{1,2} = B_1(T_d)/B_2(T_d)(\nu_1/\nu_2)^{\beta_{1,2}}$. Fits of modified black-bodies to PACS and SPIRE 160, 250, 350, 500μm data from the Herschel Gould Belt Survey (HGBS) [1] were used by [21] to create maps of dust temperature and optical extinction at 36.4″ resolution. These maps were used here.

The NIKA2 1 mm maps were convolved with a Gaussian kernel to the resolution at 2 mm, 18″, and the two maps were registered onto the same grid to create maps of the flux ratio $R_{1,2}$ and of the dust emissivity index $\beta_{1,2}(R_{1,2}, T_d)$ (Fig. 1). Positions with fluxes below 6σ were masked. In future work, we plan for a more thorough analysis of errors, taking into account the work by [17] who studied dust emissivity variations of two star-forming clouds observed with NIKA. In the present work, the $\beta_{1,2}$ maps show significant variations between ~ 1.2 and 2.4. This spread is seen in several but not all of the individual maps (Fig. 1). The core centers where the optical extinctions peak show a similar spread of $\beta_{1,2}$ values (Fig. 2). The variations of $\beta_{1,2}$ observed by us are well above the calibration errors and indicate systematic variations of the grain population emitting at mm wavelengths. Similar β values have been found in these and other cores of Taurus using also other millimeter/submillimeter cameras [3, 5, 12, 13, 20].
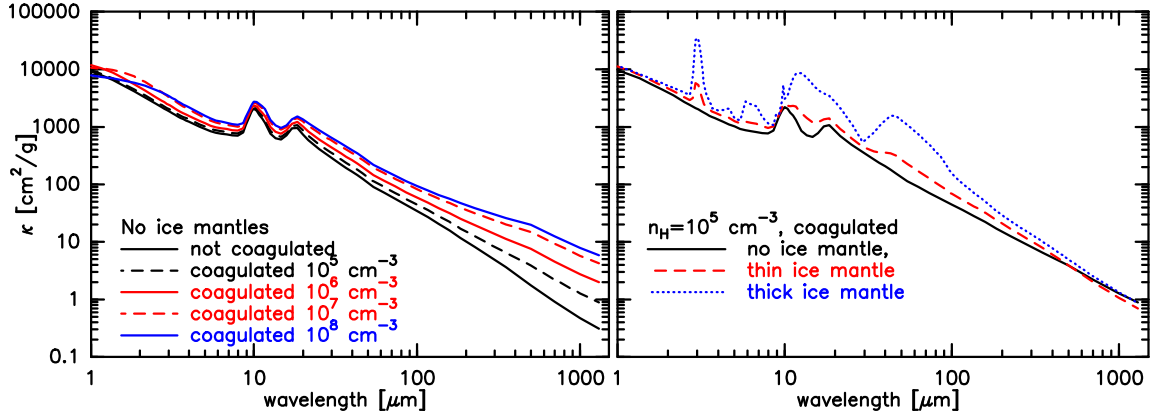
Figure 3. Modelled dust opacities [15]. **Left:** Bare grains without ice mantles, not coagulated and co-agulated with increasing hydrogen densities n_{H}. $\beta_{1.3,0.7}$ decreases from 1.74 to 1.23. **Right:** Coagulated grains with increasing ice mantle thickness at a constant hydrogen density. NIR ice features start to show-up and the dust emissivity index $\beta_{1.3,0.7}$ steepens from 1.51 to 1.89.

4 Dust opacity models

To understand these indices and their variations better, we compare with grain models. Figure 3 shows dust opacity spectra modelled by [15] for proto-stellar cores. These models assume dust grains consisting of a mixture of silicates and amorphous carbon with different levels of coagulation and ice layer coverage on the agglomerates. Starting with the Mathis-Rumpl- Nordsieck (MRN) grain size distribution [10], a coagulation period of 10^5 years is simulated. NIR/MIR wavelengths are marked by narrow silicate and ice features while submm/mm wavelengths exhibit marked variations of the slope, i.e. of the dust emissivity index β. For bare grains, the $\beta_{1.3,0.7}$ index drops from 1.74 to 1.23 with increasing density, when coagulation leads to increasingly large grains (Fig. 3, Left). On the other hand, $\beta_{1.3,0.7}$ increases with increasing thickness of the ice mantles (Fig. 3, Right) from 1.5 to 1.89 for coagulated grains and a fixed density of $n_{\mathrm{H}} = 10^5$ cm^{-3}.

5 Conclusions

Most observations of $\beta_{1,2}$ are consistent with the gradual build-up of ice mantles in the interiors of pre-stellar cores at the volume densities of $\sim 10^5$ cm^{-3} (Table 1) as predicted by grain models [15] (cf. Fig. 3, Right). In particular the radial drop of $\beta_{1,2}$ in TMC1-C fits this picture. Here, $\beta_{1,2}$ drops from ~ 2.0 at the A_V peak with ~ 16 mag to the outskirts at ~ 4 mag with $\beta_{1,2} \sim 1.1$. The region B213-C16 also fits this picture. The filamentary structure of NGC1333-C7 exhibits an almost constant $\beta_{1,2} \sim 1.6$ with the sole exception of core #2 exhibiting a much lower value of ~ 1.0. Interestingly, core #2 is a Class I protostellar object and its Deuteration, measured by the ratio of DCN/H^{13}CN abundances, is significantly lower than for the other cores of this region [12]. Its low $\beta_{1,2}$ value indicates bare grains, devoid of ice mantles, consistent with a more evolved state. The other cores of this filament are less evolved objects [7] in which CO freezes-out leading to the formation of ice mantles, and driving deuteration. The $\beta_{1,2}$ map of B213-C6 differs from the other cores. It exhibits fairly constant and high values of ~ 2.2, hardly varying with A_V. The parameter space covered by the OH94 models does however not reproduce such high $\beta_{1,2}$ values of > 2.0. See also the discussion in [20]. Alternative models to explain such high values are discussed in [9].

Acknowledgements

References

[1] P. André *et al.*, Astron. Astrophys. **518**, 102 (2010)

[2] S. Berta & R. Zylka, `piic` user manual, IRAM report (2023)

[3] A. Bracco *et al.*, Astron. Astrophys. **604**, A52 (2017)

[4] P. Caselli *al.*, Astron. Astrophys. **929**, 13 (2022)

[5] A. Chacón-Tanarro *et al.*, Astron. Astrophys. **623**, 118 (2019)

[6] A. Fuente *et al.*, Astron. Astrophys. **624**, 105 (2019)

[7] A. Hacar *et al.*, Astron. Astrophys. **606**, 123 (2017)

[8] C. Kramer *et al.*, Astron. Astrophys. **342**, 257 (1999)

[9] N. Lippok *et al.*, Astron. Astrophys. **592**, A61 (2016)

[10] J.S. Mathis *et al.*, ApJ **217**, 425 (1977)

[11] D. Navarro-Almaida *et al.*, Astron. Astrophys. **653**, A15 (2021)

[12] D. Navarro-Almaida *et al.*, Astron. Astrophys. **670**, A110 (2023)

[13] Q. Nguyen Luong *et al.*, these proceedings (2023)

[14] C.W. Ormel *et al.*, Astron. Astrophys. **532**, A43 (2011)

[15] V. Ossenkopf & T. Henning, Astron. Astrophys. **291**, 943 (1994)

[16] L. Perotto, N. Ponthieu, J.-F. Macías-Pérez, *et al.*, Astron. Astrophys. **637**, A71 (2020)

[17] A.J. Rigby *et al.*, Astron. Astrophys. **615**, A18 (2018)

[18] M. Rodriguez-Baras *et al.*, Astron. Astrophys. **648**, A120 (2021)

[19] S. Schnee *et al.*, MNRAS, **444**, 2303 (2014)

[20] S. Scibelli *et al.*, MNRAS, **521**, 4579 (2023)

[21] A. Singh & P.G. Martin *et al.*, ApJ **941**, 135 (2022)